Available online at www.sciencedirect.com
SCIENCE DIRECT®
Journal of Nuclear Materials 328 (2004) 180–196
journal of nuclear materials
www.elsevier.com/locate/jnucmat

Thermodynamic and kinetic modelling of fuel oxidation behaviour in operating defective fuel

B.J. Lewis *, W.T. Thompson, F. Akbari, D.M. Thompson, C. Thurgood, J. Higgs

Department of Chemistry and Chemical Engineering, Royal Military College of Canada, P.O. Box 17000, St. Forces, Kingston, Ont., Canada K7K 7B4

Received 22 December 2003; accepted 2 April 2004

Abstract

A theoretical treatment has been developed to predict the fuel oxidation behaviour in operating defective nuclear fuel elements. The equilibrium stoichiometry deviation in the hyper-stoichiometric fuel has been derived from thermodynamic considerations using a self-consistent set of thermodynamic properties for the U–O system, which emphasizes replication of solubilities and three-phase invariant conditions displayed in the U–O binary phase diagram. The kinetics model accounts for multi-phase transport including interstitial oxygen diffusion in the solid and gas-phase transport of hydrogen and steam in the fuel cracks. The fuel oxidation model is further coupled to a heat conduction model to account for the feedback effect of a reduced thermal conductivity in the hyper-stoichiometric fuel. A numerical solution has been developed using a finite-element technique with the FEMLAB software package. The model has been compared to available data from several in-reactor X-2 loop experiments with defective fuel conducted at the Chalk River Laboratories. The model has also been benchmarked against an O/U profile measurement for a spent defective fuel element discharged from a commercial reactor.

1. Introduction

With defective fuel, a primary leak path exists so that the primary water coolant can enter into the fuel element, permitting oxidation of both the fuel and cladding. Significant changes in the O/U ratio of the UO_{2+x} phase occur when it is exposed to oxidizing conditions. Variations in the stoichiometry result in a noticeable change in thermal conductivity of the fuel that bears directly on the thermal performance of the defective fuel element. In addition, enhanced release of volatile fission products also occurs because of the increased stoichiometry of the fuel. A mechanistic model has therefore been developed to predict the fuel oxidation behaviour in operating defective fuel elements.

Vast literature exists for the thermodynamic data in the U–O binary system. This has been well summarized in recent work [1,2] leading to construction from Gibbs energy data of the binary phase diagram. For the fuel oxidation modelling, it is important to provide in addition a self-consistent treatment to link the thermodynamic properties of all U–O phases [1,2] with equilibrium expressions for the relationship between oxygen chemical potential, temperature and UO_{2+x} non-stoichiometry [3,4]. An approach is particularly needed to link thermodynamically the U–O system with the gas-phase species (e.g., H_2/H_2O or D_2/D_2O) as well as, for instance, with condensed solutions (e.g., noble metal inclusion phases in partially-burned fuel) [5–7]. Thus, in this work, emphasis is placed on inter-related phase equilibria and the generally accepted features of the U–O binary phase diagram from room temperature to

* Corresponding author. Tel.: +1-613 5416611; fax: +1-613 5429489.
E-mail address: lewis-b@rmc.ca (B.J. Lewis).

0022-3115/$ - see front matter Crown Copyright © 2004 Published by Elsevier B.V. All rights reserved.
doi:10.1016/j.jnucmat.2004.04.336

3000 °C as boundary condition in the kinetics modelling of fuel oxidation.

The supporting thermodynamic analyses are incorporated into the model in order to determine the equilibrium state of the oxidized fuel. The fuel oxidation model can be developed from available experimental information obtained from out-of-reactor and in-reactor investigations, and tested against limited post-irradiation examination data of spent defective fuel elements from commercial reactors [8–17]. The kinetics model must specifically account for multi-phase transport including interstitial oxygen diffusion in the solid and gas-phase transport of hydrogen and steam in the fuel cracks [18,19]. The fuel oxidation model must be further coupled to a heat conduction model in order to account for complex feedback mechanisms (i.e., the stoichiometry deviation of the fuel is affected by the fuel thermal conductivity that, in turn, significantly influences the fuel temperature and thus the oxygen potential and oxidation kinetics of the fuel). The model must also consider the complicating effects of high pressure and interstitial oxygen diffusion in a temperature gradient [18–20].

2. Model development

The thermodynamic treatment in Section 2.1 can be used to provide boundary conditions for the mass-transfer modelling of the fuel oxidation process in Section 2.2. This approach provides a comprehensive treatment for describing the phenomenon of fuel oxidation in operating defective fuel elements.

2.1. O/U thermodynamic model

The current work treats the centrally important solid and liquid UO_{2+x} phases as a homogeneous equilibrium among the formal components UO_2, UO and UO_3. For the hyper-stoichiometric oxide ($x > 0$), a simple non-ideal mixing expression for the mixing of UO_2 and UO_3 brings the oxygen partial pressure into close agreement with recent reviews on the relationship between O/U ratio, temperature and oxygen partial pressure. For hypo-stoichiometric UO_{2+x} ($x < 0$), no departure terms from ideal mixing are necessary. All solid phases other than UO_{2+x} (solid and liquid) and liquid U metal (with dissolved O) are treated as stoichiometric. The U_8O_{21}, U_3O_{8-x}, $\alpha' U_3O_8$ phases are collectively treated as U_3O_8. Also the small variation in the U_4O_9 stoichiometry as it approaches 1130 °C is ignored. These simplifications are the same as those made in other recently published treatments [1,2]. Minor adjustments to the enthalpies of formation (within experimental uncertainty) have been sufficient to ensure self-consistency among potentially co-existing phases. The metallic uranium liquid phase makes allowance for dissolved atomic oxygen. The treatment is considered valid from 25 to 3000 °C and provides explicit expressions for partial oxygen pressure for all phase combinations in this range.

The low-temperature part of the phase diagram must be adequately treated since low-temperature situations arise with defective fuel transfer and storage in pools. Such effects are particularly important since post-irradiation data are inevitably used for validation of models specifically developed to describe (in-reactor) fuel oxidation behaviour (see Section 4). Fuel melting can also occur in defective fuel under normal operating conditions as the liquidus and solidus temperatures are reduced by several hundreds of degrees in hyper-stoichiometric fuel (see Section 2.1.2).

A key feature in the modelling approach for the U–O system has been the provision to connect it with thermodynamic treatments (existing or under development) for other compounds and phases so that, for example, the influence of fission products on the fuel oxidation state can be evaluated via a unifying methodology (i.e., as other elemental products are produced in the fission process as the fuel is burned up).

2.1.1. Uraninite phase 'UO_2'

The departure from stoichiometry for this phase from the ideal UO_2 has been variously expressed in terms of the atom fraction of O or U, the O/U ratio, or the value of x in the subscript UO_{2+x}. A value of x greater or less than zero is generally termed hyper- or hypo-stoichiometry, respectively. Hyper-stoichiometry may be envisioned for modelling purposes as a solid solution of stoichiometric UO_2 with a hypothetical (formal) dissolved component 'UO_3' having the uraninite (fluorite) structure. This formal component is not to be confused with pure solid uranium trioxide, UO_3, which does not have the fluorite structure. In the same way, hypo-stoichiometry can be envisioned as a solid solution of ideal UO_2 with a hypothetical (formal) dissolved component 'UO' with the fluorite structure. Thus, for thermodynamic modelling purposes, uraninite can be regarded as a solid solution of component oxides each with a different oxidation state (U^{2+}, U^{4+}, U^{6+}) governed by homogeneous equilibria influenced by oxygen partial pressure. On the hyper-stoichiometric side, the concentration of 'UO' is virtually nil so the controlling equilibrium may be expressed as

$$2UO_2 + O_2 = 2\text{'}UO_3\text{'} \quad (1)$$

On the hypo-stoichiometric side, the concentration of 'UO_3' is negligible so the controlling equilibrium may be regarded as

$$2\text{'}UO\text{'} + O_2 = 2UO_2 \quad (2)$$

Contact with oxygen (perhaps controlled in partial pressure by an H_2/H_2O mixture) disturbs the homogeneous equilibrium in ideal UO_2 to make it hypo- or hyper-stoichiometric by the development of dissolved 'UO' or 'UO_3', respectively. The mole fraction of 'UO' or 'UO_3' thus is no more than another way of expressing non-stoichiometry justified only by it providing a useful thermodynamic treatment. Of course, the approach must also make possible the proper placement of the calculated phase boundaries surrounding the 'UO_2' field.

For *hyper-stoichiometry*, composition equivalents are:

$$\text{O/U atom ratio } r \quad r = 2 + X_{UO_3}, \tag{3}$$

$$UO_{2+x} \quad x = X_{UO_3}, \tag{4}$$

$$\text{atom fraction O} \quad X_O = (2 + X_{UO_3})/(3 + X_{UO_3}), \tag{5}$$

where, for these equivalent definitions, r is the O/U ratio, X_{UO_3} is the mole fraction of UO_3 and x is the stoichiometry deviation in UO_{2+x}. Analogously, for *hypo-stoichiometry*, composition equivalents are:

$$\text{O/U atom ratio } r \quad r = 2 - X_{UO}, \tag{6}$$

$$UO_{2-x} \quad x = X_{UO}, \tag{7}$$

$$\text{atom fraction O} \quad X_O = (2 - X_{UO})/(3 - X_{UO}). \tag{8}$$

Since the maximum departure from non-stoichiometry is greater in the hyper-stoichiometric sense, it is appropriate to consider first the homogeneous equilibrium in Eq. (1):

$$\begin{aligned}\Delta G_1^o &= -RT \ln K_{eq} \\ &= -2RT \ln a_{UO_3} + 2RT \ln a_{UO_2} + RT \ln P_{O_2},\end{aligned} \tag{9}$$

where ΔG_1^o is the standard Gibbs energy change for the corresponding complete reaction, R is the ideal gas constant, T is the temperature and P_{O_2} is the oxygen partial pressure. Expressing the activities, a, with activity coefficients, γ, or partial excess Gibbs energies, G^E, gives

$$\begin{aligned}RT \ln a_{UO_3} &= RT \ln X_{UO_3} + RT \ln \gamma_{UO_3} \\ &= RT \ln X_{UO_3} + \overline{G}^E_{UO_3},\end{aligned} \tag{10}$$

$$\begin{aligned}RT \ln a_{UO_2} &= RT \ln X_{UO_2} + RT \ln \gamma_{UO_2} \\ &= RT \ln X_{UO_2} + \overline{G}^E_{UO_2}.\end{aligned} \tag{11}$$

The term $\overline{G}^E_{UO_3}$ depends on composition, which can be expressed with a series of the type:

$$\overline{G}^E_{UO_3} = (X_{UO_2})^2[p_0 + 2p_1 X_{UO_3} + 3p_2 (X_{UO_3})^2 + \cdots], \tag{12}$$

where the p_i coefficients are adjustable constants (fit to experimental data). The partial excess Gibbs energies for each component are related by the Gibbs–Duhem equation at any particular temperature:

$$X_{UO_2} \, d\overline{G}^E_{UO_2} + X_{UO_3} \, d\overline{G}^E_{UO_3} = 0. \tag{13}$$

Thus, with coefficients arranged as in Eq. (12), $\overline{G}^E_{UO_2}$ is expressed as

$$\begin{aligned}\overline{G}^E_{UO_2} = (X_{UO_3})^2[&(p_0 - p_1) + (2p_1 - 2p_2)X_{UO_3} \\ &+ (3p_2 - \cdots)(X_{UO_3})^2 + \cdots].\end{aligned} \tag{14}$$

Combining Eqs. (10)–(12) and (14) with (9), yields

$$\begin{aligned}\Delta G_1^o = &RT \ln P_{O_2} + RT \ln(X^2_{UO_2}/X^2_{UO_3}) \\ &+ 2\{-p_0 + [2p_0 - 2p_1]X_{UO_3} + [3p_1 - 3p_2]X^2_{UO_3} \\ &+ [4p_2 - \cdots]X^3_{UO_3} + \cdots\}.\end{aligned} \tag{15}$$

Eq. (15) provides the basis for fitting non-stoichiometry (from Eq. (4) expressed as X_{UO_3}) to oxygen pressure. The adjustable parameters are the temperature coefficients in the expression for ΔG_1^o and the coefficients p_i expressed as linear functions of T. In the present treatment, the expansion of the partial excess Gibbs energies was truncated at three coefficients since this was deemed sufficient to fit the scatter of experimental measurements.

A similar treatment for the hypo-stoichiometric side did not require any partial excess Gibbs energy terms for the component oxides. The only adjustable parameter was the expression for ΔG_2^o or, equivalently, the standard Gibbs energy of formation of the hypothetical 'UO' component with the fluorite structure in Eq. (2).

In order to judge the current representation, the calculated oxygen partial pressures are shown in Fig. 1 at 1473 K. Fig. 2, at the higher temperature of 1973 K, extends more into hypo-stoichiometry. At the extreme of hyper-stoichiometry in Fig. 2, the oxygen partial pressure is nearly 1 atm since this temperature is near the decomposition of U_3O_8 shown in Eq. (16) (Section 2.1.2).

2.1.2. Computed U–O phase diagram

The modelling treatment for UO_2 described in Section 2.1.1, together with a similar one of the analogous molten 'UO_2' phase, is the foundation of a computation of the U–O binary phase diagram by Gibbs energy minimization. To this analysis was added a regular solution treatment for dissolved O in molten U metal. The remaining thermodynamic data requirements are the properties of the solid stoichiometric oxide phases, notably U_4O_9, U_3O_8 and pure UO_3. There is no major dispute about the Gibbs energies of formation of these oxides but the computed phase diagram is very sensitive to small changes in these properties. Accordingly, minor adjustments to Gibbs energies of formation within the known uncertainties were made in order to give overriding importance to temperatures of decomposition such as

$$U_3O_8 = 3\text{'}UO_2\text{'} + O_2 \tag{16}$$

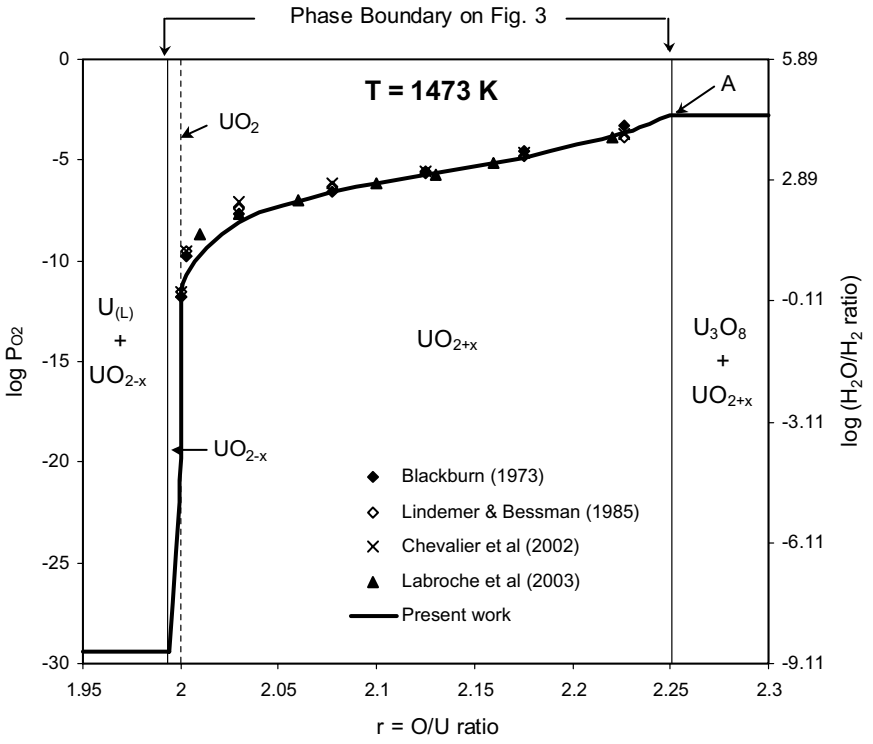

Fig. 1. Partial oxygen pressure (atm) in 'UO_2' at 1473 K.

The calculated U–O system resulting from this evaluation/modelling process is shown in Fig. 3 along with measured solubilities from several sources. Generally, most measurements have been melded together except for the O solubility measurements of Wang in molten U [21]. As in other recent evaluations [1,2], the lower oxygen solubility has been accepted and parameters have been adjusted, accordingly. An effort was made to place the irregular phase boundary for 'UO_2' saturation with U_4O_9 although several terms in the expression for ΔG_1^o were necessary. Estimates were also made for the properties of U_3O_7 so that it would decompose at the temperature shown. U_3O_7 is not shown as a separate phase in the other recent evaluations [1,2]. Gaseous oxides (UO and UO_3 as well as metal vapour) are also included in the current treatment but these species generally have quite low partial pressures except for UO_3 vapour near the melting of UO_2. The standard thermodynamic properties settled upon for all U–O species in the current evaluation are given in Table 1. These are in close accord, although not exactly the same, as data in recent reviews [1,2].

2.1.3. Representation of partial oxygen pressure

The principal use for thermodynamic data in connection with fuel oxidation modelling is the computation of the partial oxygen pressure. A typical situation considers uranium oxide(s) in contact with gas mixtures of H_2 and H_2O, which fixes the P_{O_2} at any specified temperature. The thermodynamic data leading to Figs. 1–3 is expressed as equations for $\log_{10} P_{O_2}$ in Table 2. The equations relate to the numbered regions on Fig. 4. In the two-phase regions, (P_{O_2}) is a function only of temperature following the dictates of the Gibbs Phase Rule. In the non-stoichiometric single phase areas, the O/U ratio, r, is also part of the functional form. Thus, the non-stoichiometry limit for UO_{2+x} at, say, the temperature of Fig. 1 (1473 K) could be obtained by finding $\log P_{O_2}$ for region 5 in Fig. 4, and then finding r for region 14 using the same value for $\log P_{O_2}$. The embedding of this table into a computer model is the basis for connecting, in a self-consistent way, thermodynamics to mass-transfer modelling. This approach circumvents the need to perform first principle iterative Gibbs energy minimization calculations in a mass-transfer model (Section 2.2), thereby considerably accelerating those computations.

Fig. 5 shows a comparison of the data in Table 2 with the recent work of Labroche et al. [22]. This comparison shows phase stability in $\log P_{O_2} - 1/T$ co-ordinates near a triple point of significance in fuel oxidation: UO_{2+x}, U_3O_8 and U_4O_9. The solid lines derive from Table 2. A

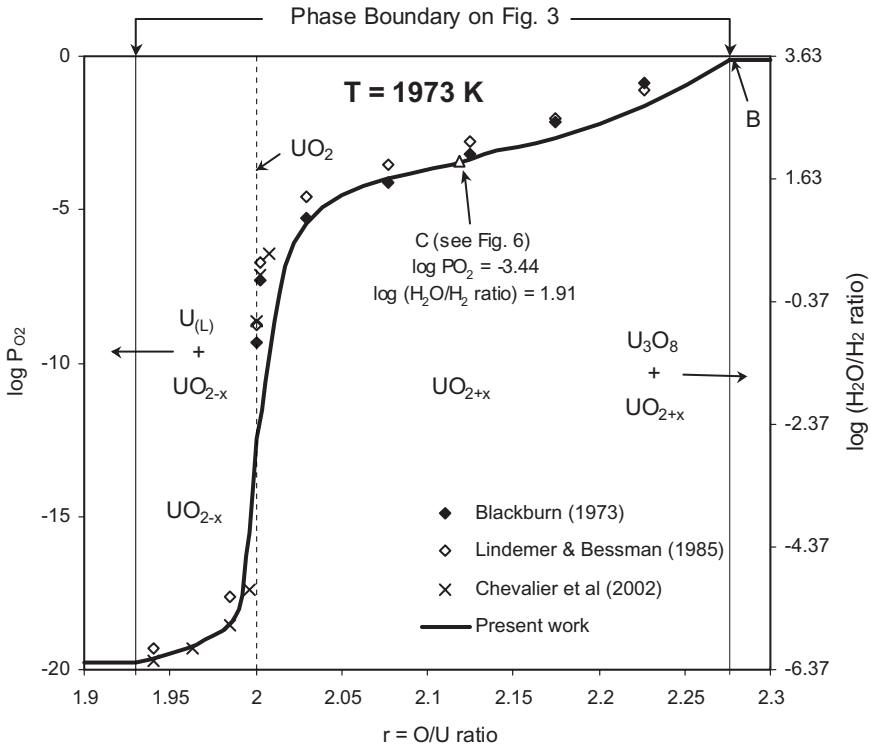

Fig. 2. Partial oxygen pressure (atm) in 'UO_2' at 1973 K. Emphasis was placed on the partial oxygen pressure at B in locating the right hand extreme.

comparison of available data with the calculated phase diagram for the U–O system is also shown in Fig. 3 [22–36].

2.1.4. Application of U–O thermodynamic data

Fig. 6 shows the realization of the objective of the U–O modelling (i.e., as stated in Section 1), which shows the linkage of the U–O model to data on gaseous H_2O, H_2, O_2, UO_3, UO_3 (H_2O). This figure shows the consequences of exposing stoichiometric UO_2 to water vapour at 1973 K at a high pressure (i.e., typical of defective-fuel operation at 100 atm). An arbitrary proportion of UO_2 to H_2O of 1:10 was used in this sample output to underline that such closed-system calculations are sensitive to initial proportions (excess H_2O dilutes the other gases which form). The process of Gibbs energy minimization was used to determine the most stable products [5]. This calculation affirms that the dominant reaction is $UO_2+xH_2O \rightarrow UO_{2+x}+xH_2$. The degree of non-stoichiometry developed in 'UO_2' fuel and the related partial O_2 pressure ($100\times0.37046\times10^{-5}=3.7\times10^{-4}$ atm = 37 Pa) as governed by the H_2/H_2O equilibrium are consistent with the phase diagram in Fig. 3 and the data in Table 2. The small UO_3 partial pressure ($100\times0.15944\times10^{-5}=1.6\times10^{-4}$ atm = 16 Pa) provided as a by-product of this general computational method gives assurance that oxidation kinetics models developed in Section 2.2 are indeed focused on the dominant oxidation reaction. Other possible phases considered in the computation, but not part of the most stable phase assemblage (represented in Fig. 6 by U_4O_9), show their activities in order to better judge the nearness to precipitation (i.e., where the activity $a = 1$).

Finally, the treatment in Section 2.1.1 and Fig. 6 (whereby non-stoichiometric 'UO_2' is viewed as a solution with hypothetical 'UO' and 'UO_3' solutes) opens the way to introduce fission products into the fuel in further model development that is underway. All of the current U–O treatment can be used in conjunction with other thermodynamic treatments of 'noble metal' fission products (Mo,Tc, Ru, Rh, Pd) and Zr–Sn cladding alloy previously developed [7].

The application of the thermodynamics model (i.e., Table 2) to fuel oxidation kinetics modelling is described in Section 2.2.

2.2. Fuel oxidation kinetics model

During in-reactor operation, a temperature gradient develops due to internal fission heating. Steam present in

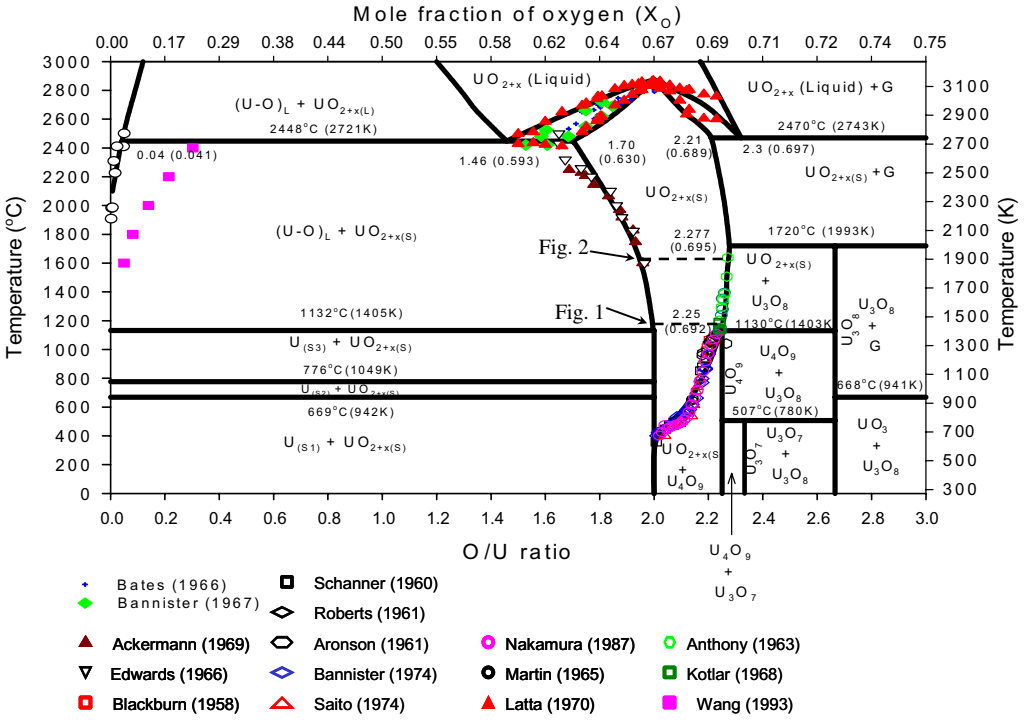

Fig. 3. Calculated phase diagram for the U–O system shown against direct experimental phase boundary determinations.

Table 1
Standard thermodynamic properties of species in U–O system

Species	$\Delta H^0_{298.15}$ (J mol^{-1})	$S^0_{298.15}$ (J mol^{-1} K^{-1})	C_p (J mol^{-1} K^{-1})	Temp. range (K)
U (orthorhombic)	0.0	50.291680	$26.9198560 - 0.250203200 \times 10^{-2}T - 76985.6T^{-2} + 0.2655794 \times 10^{4}T^{2}$	298–942
	−4316.85	40.478249	42.92784	942–5000
(tetragonal)	2790.73	53.254236	$26.9198560 - 0.250203200 \times 10^{-2}T - 76985.6T^{-2} + 0.2655794 \times 10^{4}T^{2}$	298–942
	−1526.12	43.440805	42.92784	942–1049
	1961.00	49.283240	38.28360	1049–5000
(cubic)	3231.08	47.975798	42.92784	298.1–1049
	6718.21	53.818233	38.2836	1049–1405
UO_2 (solid)	−1 084 910	77.821998	$52.1743 + 0.087951T - 0.842411 \times 10^{-4}T^{2} + 0.31542 \times 10^{-7}T^{3} - 0.26334 \times 10^{-11}T^{4} - 713910T^{-2}$	298–3120
U_4O_9 (solid)	−4 529 705.72	334.0924	$319.163 + 0.049691T - 3960200T^{-2}$	298–850
	−4 527 385.95	338.212645	$281.5 + 0.088836T - 1175737.6T^{-2}$	850–1397.5
	−4 138 251.79	864.382995	$20.0/T$	1397.5–3500
U_3O_7 (solid)	−3 437 715.95	250.194300	$250.0T$	298–800
U_3O_8 (solid)	−3 583 350.58	282.42	$265.423470 + 0.049381T - 0.29931 \times 10^{-5}T^{2} - 3537016.4T^{-2}$	298–2148
UO_3 (solid)	−1 228 384.79	96.106488	$88.70 + 0.01449T - 10090000T^{-2}$	298–2000

the fuel-to-clad gap of a defective fuel rod can penetrate through cracks in the pellet by gas-phase transport and react with the fuel resulting in an oxygen profile in the pellet since the thermodynamics of the oxidation reaction is temperature dependent. A re-distribution of the interstitial oxygen ions can also occur due to solid-state

Table 2
Complete set of the oxygen partial pressure equations for the U–O binary system

Region[a]	Equations for $\log_{10} P_{O_2}$	Temp. (K)	$R = O/U$ ratio
1	$-6.03 - 9323.47/T + 5.4\log T$	298–941	$2.67 < r < 3.0$
2	$16.84 - 16317.56/T - 2.83\log T$	298–780	$2.33 < r < 2.67$
3	$-24.70 - 14176.71/T + 10.52\log T$	298–780	$2.25 < r < 2.33$
4	$10.89 - 16140.69/T - 0.87\log T$	780–1403	$2.25 < r < 2.67$
5	$28.34 - 19877.41/T - 5.57\log T$	1403–1993	$* < r < 2.67$
6	$11.44 - 56650.96/T - 0.83\log T$	298–942	$0 < r < 2$
7	$-1.178 - 55219.47/T + 2.90\log T$	942–1049	$0 < r < 2$
8	$15.26 - 57512.74/T - 1.82\log T$	1049–1405	$0 < r < 2$
9	$16.76 - 58233.09/T - 2.13\log T$	1405–2721	$0 < r < *$
10	$-8.36 - 44928.73/T + 3.76\log T$	2721–3200	$* < r < *$
11	$-1753.55 + 465961.96/T + 457.23\log T$	2721–3100	$* < r < *$
12	$1696.89 - 497801.46/T - 440.82\log T$	2743–3100	$* < r < *$
13	$-19.90 - 15681.39/T + 8.64\log T$	298–600	$2 < r < 2.25$
		600–1403	$* < r < 2.25$
14	$-19134.68 + 3456557.40/T + 5460.56\log(T) - 584250192/T^2$ $-2\log((3-r)/(r-2))$ $-(0.104/T)(1094082 - 365288(r-2) + 2259561(r-2)^2 - 6658500(r-2)^3)$	600–800	$2.0 \leqslant r < *$
	$-285.7 - 0.02T + 115454.42/T + 97.51\log(T) - 2\log((3-r)/(r-2))$ $-(0.104/T)(1094082 - 365288(r-2) + 2259561(r-2)^2 - 6658500(r-2)^3)$	800–1400	
	$15.6 + 92718.93/T - 2.23\log(T) - 2\log((3-r)/(r-2))$ $-(0.104/T)(1094082 - 365288(r-2) + 2259561(r-2)^2 - 6658500(r-2)^3)$	1400–3100	
15	$-2\log((2-r)/(r-1)) + 17.55 - 67632.79/T - 1.57\log T$	1200–3000	$* < r < 2.0$
16	$-2\log((2-r)/(r-1)) + 1871.37 - 651954.74/T - 478.5\log T$	2721–3100	$2.0 < r < *$
17	$-2\log((3-r)/(r-2)) + [819.92 - 2519579.3/T]r$ $-14436.69 + 9663388.98/T + 3237.34\log T$	2743–3100	$0 < r < *$
18	$2[\log(r/(r+1)) + (43400.81r - 4736.08)/T - 3.52]$	2500–3100	$0 < r < *$

(*) Fig. 4 should be used to find the boundary range.
[a] Regions correspond to those labeled in Fig. 4. Note $r = O/U$ ratio.

diffusion. Any hydrogen generated from both the Zircaloy clad and fuel oxidation processes will also affect the oxygen potential in the gaseous atmosphere.

The transport delivery mechanism is therefore a complicated problem where gas and solid-state radial diffusion equations must be coupled by a kinetically-limited reaction law at the crack surfaces (see Fig. 7). In particular, the H_2O/H_2 gas mixture in the gap will diffuse radially through a network of cracks where a reaction occurs with the solid fuel. The reaction products, consisting of H_2 in the gas in the cracks and interstitial oxygen ions in the solid fuel, are then transported via diffusion in their respective phase (Fig. 7). Due to the lower fuel surface temperature, the outer pellet surface will remain essentially stoichiometric.

The rate of reaction of UO_{2+x} with a gas mixture containing steam and hydrogen at partial pressures of $p_{H_2O} = (1-q)p_t$ and $p_{H_2} = qp_t$ is given by [18]

$$R_{ox} = c_U \alpha \sqrt{(1-q)p_t}(x_e - x(t)), \tag{17}$$

where R_{ox} is the reaction rate in moles O (or H_2) $m^{-2}\,s^{-1}$, $c_U = 4.1 \times 10^4$ mol m^{-3} is the molar density of uranium in UO_2, $\alpha = 0.365\exp(-23500/T)$ (in $m\,s^{-1}$) is the surface-exchange coefficient [11,12] at temperature T (in K), q is the mole fraction of H_2 in the cracks and $p_t = 100$ atm is the total system pressure. The equilibrium oxidation state of the fuel x_e can be obtained by equating the oxygen partial pressure in the local atmosphere with the oxygen partial pressure in the solid fuel (Table 2). The oxygen partial pressure p_{O_2} (atm) in the atmosphere can be obtained from a solution of the cubic equation [18]:

$$4(p_{O_2})^3 + 4[(p_{H_2})_i - K_2^*]p_{o_2}^2 + [(p_{H_2}^2)_i + 4(p_{H_2O})_i K_2^*]p_{O_2} - (p_{H_2O}^2)_i K_2^* = 0, \tag{18}$$

where $(p_{H_2O})_i$ and $(p_{H_2})_i$ are the initial steam and hydrogen partial pressure quantities and the equilibrium constant K_2^* for water dissociation is given by [37]

$$\log K_2^* = -\frac{25032}{T} + 1.9588\log T - 0.96630. \tag{19}$$

The solution of Eq. (18) can be equated to the oxygen partial pressure formulation for the UO_{2+x} region 14 in

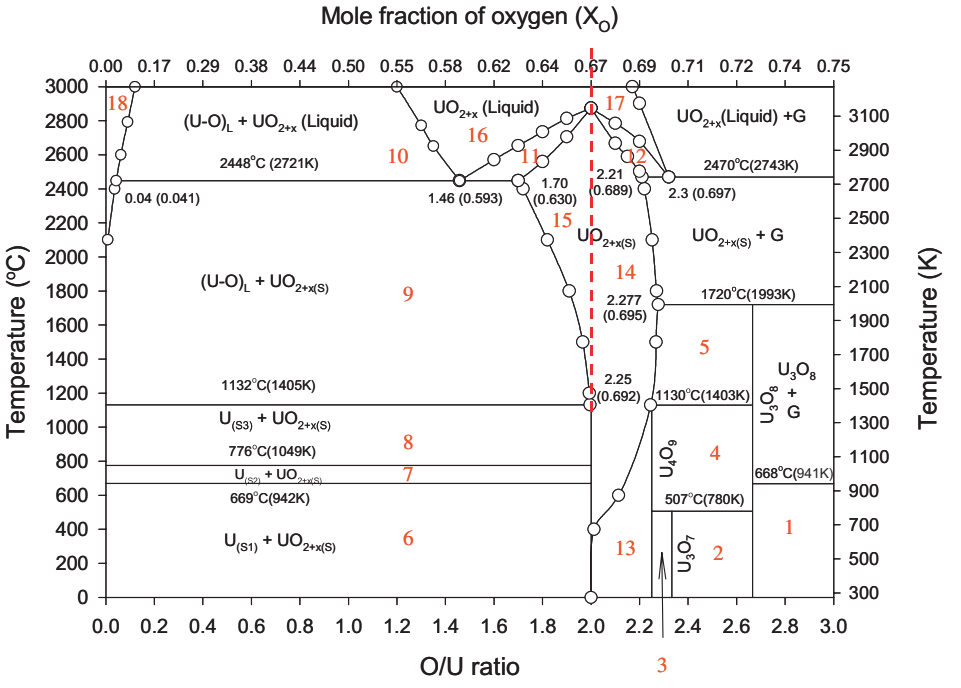

Fig. 4. 'Region' key for use with Table 2, which provides thermodynamic data in a form suitable for direct use in oxidation calculations.

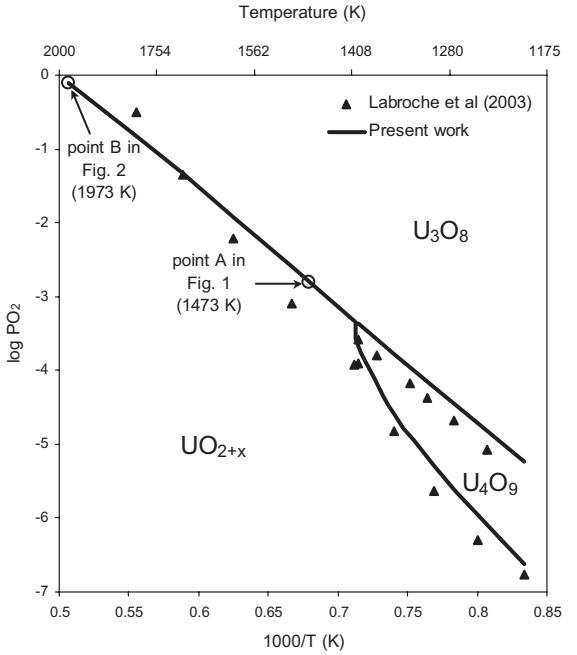

Fig. 5. Comparison of data in Table 2 with data of Labroche et al.

Fig. 4 and Table 2. Thus, x_e can be solved for by utilizing the thermodynamic analysis in Section 2.1 (where $x_e = r - 2$ via Eqs. (3) and (4)).

With the fuel oxidation reaction, $UO_2 + xH_2O \rightarrow UO_{2+x} + xH_2$, the transport equation for O diffusion in the fuel pellet is given by

$$c_U \frac{\partial x}{\partial t} = c_U \vec{\nabla} \cdot (D \vec{\nabla} x) + \sigma R_{ox}, \tag{20}$$

where σ is the surface area of cracks per unit volume of fuel (m^{-1}) for the cracked fuel body. Here D is taken as the chemical diffusion coefficient for oxygen [38]:

$$D = 2.5 \times 10^{-4} \exp\left(-\frac{16400}{T}\right) m^2 s^{-1}. \tag{21}$$

The diffusion coefficient in Eq. (20) cannot be assumed to be independent of position because of the strong temperature dependence. Thus, assuming only radial diffusion in a cylindrical fuel pellet of radius a_p, Eq. (20) becomes

$$\frac{\partial x}{\partial t} = \sigma \alpha \sqrt{(1-q)p_t}\{x_e - x(t)\} + \frac{1}{r}\left[\frac{\partial}{\partial r}\left(Dr\frac{\partial x}{\partial r}\right)\right]. \tag{22}$$

The fuel pellet is initially assumed to be stoichiometric:

$$x = 0, \quad 0 \leqslant r \leqslant a_p, \quad t = 0. \tag{23a}$$

UO_2 + 10 H_2O → (to yield most stable products **at 1973 K and 100 atm**.)

10.001 mol	(	0.98790	H_2O	
total mols	+	0.11963×10^{-1}	H_2	
of gas	+	0.11751×10^{-3}	OH	*equilibrium mole*
	+	0.14682×10^{-4}	H	*fractions precede species*
	+	0.37046×10^{-5}	O_2	
	+	0.16778×10^{-5}	$UO_3(H_2O)$	
	+	0.15944×10^{-5}	UO_3	
	+	0.10369×10^{-6}	O)	
			(Gas)	
+ **0.99997** mol	(	0.88098	UO_2	*hyper-stoichiometric oxide*
	+	0.11902	UO_3	
	+	0.16877×10^{-12}	UO)	
			(Solid, $UO_{2.11902}$)	
+ **0.00000** mol U_4O_9				*considered but does not form*
			(Solid, a = 0.48735)	

Fig. 6. Illustration of linkage of U–O model to gaseous H–O data to conduct a computation of interest to fuel oxidation kinetics. The most stable products of the reaction between 1 mol of initially stoichiometric UO_2 and 10 mol of H_2O in a *closed system* at 1973 K and 100 atm have been found by Gibbs energy minimization. The calculation corresponds to point C in Fig. 2.

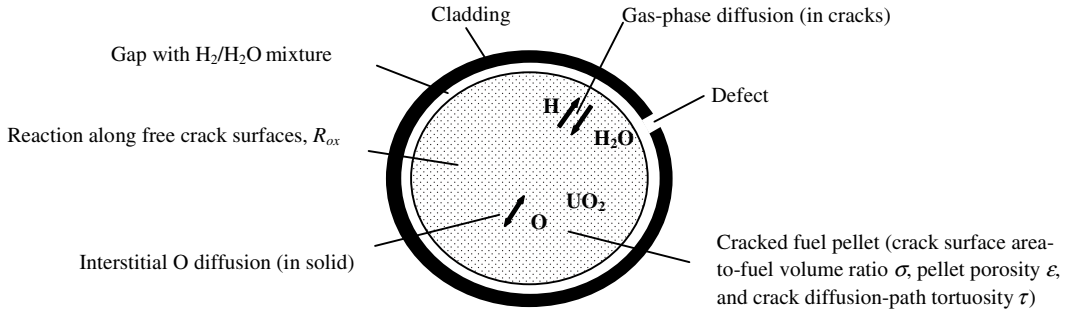

Fig. 7. Schematic for defective fuel oxidation model.

Symmetry is considered with the use of a reflexive boundary condition at the centre of the pellet:

$$\frac{\partial x}{\partial r} = 0, \quad r = 0, \quad t > 0. \tag{23b}$$

At the surface of the pellet, where the temperature is lower, the fuel essentially remains stoichiometric so that:

$$x \approx 0, \quad r = a_p, \quad t > 0. \tag{23c}$$

In previous work, the hydrogen-to-steam ratio was fixed and assumed to remain constant throughout the pellet [18]. However, in this analysis, the impact of hydrogen generation from the fuel oxidation process is modelled by including a diffusion equation for the hydrogen mole fraction q in the cracked fuel body (see Fig. 7). The cracked solid is assumed to have a porosity, defined as the ratio of the volume of cracks (and/or pores) to that of the solid fuel i.e., $V_{\text{cracks}}/V_{\text{fuel}}$. Thus, as follows from the mass balance, the hydrogen molar concentration $(c_g q)$ in the cracks is given by [19]

$$\varepsilon \frac{\partial (c_g q)}{\partial t} = \varepsilon \vec{\nabla} \cdot (c_g D_g \vec{\nabla} q) + \sigma R_{ox}, \tag{24}$$

where c_g is the total molar concentration of gas ($\text{mol}\,\text{m}^{-3}$) (assumed to be ideal) ($= p_t/RT$ and $R = 82.057 \times 10^{-6}$ $\text{m}^3\,\text{atm}\,\text{mol}^{-1}\,\text{K}^{-1}$ is the ideal gas constant). Equivalently, for radial diffusion with a tortuosity factor τ for the diffusion path in the cracked solid, Eq. (24) becomes

$$\varepsilon c_g \frac{\partial q}{\partial t} = c_U \sigma \alpha \sqrt{(1-q)p_t}\{x_e - x(t)\} + \frac{\varepsilon}{\tau^2 r}\left[\frac{\partial}{\partial r}\left(c_g D_g r \frac{\partial q}{\partial r}\right)\right]. \quad (25)$$

In the development of Eq. (25), a quasi-static assumption has been used for the total molar concentration [19]. The quantity $c_g D_g$ (in mol m^{-1} s^{-1}) is evaluated from the Chapman–Enskog kinetic theory for gases [39]:

$$cD_g = 2.2646 \times 10^{-3} \frac{\sqrt{T\left(\frac{1}{M_{H_2}} + \frac{1}{M_{H_2O}}\right)}}{\sigma_{AB}^2 \Omega_{AB}}, \quad (26)$$

where T is the temperature (K), M is the molecular weight (in g mol^{-1}), σ_{AB} (Å) is the combined collision diameter and Ω_{AB} is the collision integral. The combined parameters are evaluated from individual Lennard-Jones force constants for H_2 and H_2O [39,40].

Eq. (25) is subject to the initial condition:

$$q = q_1, \quad 0 \leqslant r \leqslant a_p, \quad t = 0, \quad (27a)$$

where q_1 is taken as an initial hydrogen mole fraction in the fuel-to-clad gap. Symmetry at the centre of the pellet is again considered with the use of a reflexive boundary condition:

$$\frac{\partial q}{\partial r} = 0, \quad r = 0, \quad t > 0. \quad (27b)$$

At the surface of the pellet, hydrogen is present in the fuel-to-clad gap due, for instance, to the Zircaloy oxidation process. Thus, in the current analysis, it is assumed that the hydrogen mole fraction is again equal to a constant value of q_1:

$$q = q_1, \quad r = a_p, \quad t > 0. \quad (27c)$$

For a solution of these transport equations, the temperature profile must also be known, which can be obtained from the (steady-state) heat conduction equation [41]

$$\rho C_p \frac{\partial T}{\partial t} = \frac{1}{r}\frac{\partial}{\partial r}\left(rk\frac{\partial T}{\partial r}\right) + \frac{P}{\pi a^2}\left[\frac{(\kappa a_p)}{2I_1(\kappa a_p)}\right] I_0(\kappa r) = 0. \quad (28)$$

Here k is the thermal conductivity, ρ is the density and C_p is the specific heat for the solid, P is the linear power of the fuel rod and κ is the inverse neutron diffusion length (e.g., $\kappa = 1.1$ cm^{-1} for naturally-enriched fuel at 8000 MWd t^{-1}). Eq. (28) is further coupled to the other two partial differential equations because the thermal conductivity is also a function of x. The thermal conductivity model is taken from Ref. [18] and employs the Ellis, Porter and Shaw model for the phonon contribution [42]. Similarly, Eq. (28) is subject to the conditions:

$$\frac{\partial T}{\partial r} = 0, \quad r = 0, \quad t > 0 \quad (29a)$$

and

$$T = T_l, \quad r = a_p, \quad t > 0, \quad (29b)$$

where T_l is the fuel surface temperature. A steady-state heat conduction equation is considered in the current treatment since a steady-state temperature distribution is quickly approached under normal operating conditions. To account for the effects of a reduced heat transfer in the fuel-to-sheath gap and pellet expansion due to thermal effects, the fuel surface temperature T_l was estimated from a previous simulation of the various X-2 defect fuel experiments with the ELESIM fuel performance code (Section 3.1) [8,9].

3. Results

The system of partial differential equations in Section 2.2 are solved numerically using a finite-element method with the commercial FEMLAB software package (Version 2.3) [43]. The simulations are compared to gravimetric data of the average O/U ratio derived from in-reactor loop experiments with defective fuel rods at the Chalk River Laboratories (CRL) (Sections 3.1) and with oxygen profile data for a commercial spent defective rod (Section 3.2).

3.1. Simulation of CRL defect experiments

Various experiments were conducted in the X-2 defect loop at the CRL with artificially (Table 3(panel A)) and naturally-defective (Table 3(panel B)) fuel elements, as detailed in Ref. [8]. In this analysis, defect experiments FDO-687, FFO-103, FFO-102-2 and FFO-104 have been considered since measured O/U data are available or it is suggested that fuel centreline melting has perhaps been observed in the ceramographic examinations. The model input for these experiments are detailed in Table 4. A comparison of the simulation results with experimental observations is also summarized in Table 4. The predicted profiles of the hydrogen mole fractions, stoichiometry deviations and fuel temperatures are shown in Fig. 8(a)–(d).

For the current analysis, ε is estimated from $1 - \rho/\rho_{TD}$, where ρ is the density of the UO_2 fuel ($\sim$10.7 g cm^{-3}) and ρ_{TD} is the theoretical density of the fuel ($= 10.96$ g cm^{-3}). From the results of out-of-pile experiments the crack surface area-to-fuel volume σ was taken as three times the geometric surface-to-volume ratio of the fuel (i.e., $\sigma = 1350$ m^{-1}) [10]. This parameter determines how quickly the equilibrium stoichiometry deviation is reached; however, the model is not overly sensitive to this quantity since equilibrium was quickly

Table 3
Summary of experiments with single defected fuel elements at CRL

Experiment (element)	Defect description	Drilled/machined defect location and size (mm^2)			Linear power ($kW\,m^{-1}$)	Burnup ($MWh\,kg^{-1}\,U^{-1}$)		Defect residence time (effective full power days)	Irradiation date
		Location (mm)[a]	Initial	Final		Initial	Final		
Panel A: Artificially-defected fuel									
FDO-681									
Phase I (RPL)	Single drilled hole (1.3 mm)[b]	102	1.3	1.3	49	140[c]	158	15	1975 Jul 24 to Aug 10
Phase II (LFZ)	Single drilled hole (1.2 mm)[b]	102	1.1	1.1	48	0	20	24	1975 Aug 10 to Sep 23
Phase III (RPP)	Two drilled holes (1.3 and 0.4 mm)[b]	101, 110	1.5	1.5	47	140[c]	173	35	1975 Oct 8 to Nov 16
FDO-687									
Phase I (RPR)	Single drilled hole (2.0 mm)[b]	100	3.1	3.1	55	43[c]	85	40	1976 Mar 13 to Apr 25
Phase II (NSZ)	Slit (10 mm × 0.6 mm)[b]	78.5	6.0	6.0	58	0	28	26	1976 Apr 30 to May 26
Phase III (RPR)	Three drilled holes[d]	35, 100, 159	7.2	7.2	54	85	90	4	1976 Jun 10 to Jun 14
FFO-103 (A3N)	23 through-wall slits in a helical pattern along sheath (each slit 36 mm × 0.3 mm)	–	272	1490[e]	48	0	18	15	1981 May 30 to Jun 14
Panel B: Naturally-defected fuel									
	Test (defect) description	Defect size (mm^2)							
		Initial	Final						
FFO-102-2 (A7E)	Reirradiation of element with through-wall hydriding at high power (cracked hydride blisters at one end of element)	11	300[f]		67	37	67	19	1981 Mar 17 to Apr 5
FFO-104 (A2F)	Power ramp failure by stress-corrosion cracking (nine randomly located, small hydride cracks)	0.00[g]	45[f]		26 (soak) 58 (ramp)	255	278	16	1981 May 6 to May 24

[a] Distance of defect from top end plug shoulder.
[b] Located at element mid-length.
[c] Irradiated intact to this burnup.
[d] Two additional 1.6 mm holes were drilled, with each hole equidistant from the ends of the fuel stack length.
[e] Slits enlarged during irradiation due to fuel expansion (defect size estimated from post-irradiation examination).
[f] Defect sizes estimated from post-irradiation examination.
[g] Element A2F was initially intact, but failed in-reactor following a power ramp.

Table 4
Parameters for the simulation of the X-2 experiments and commercial spent defective element irradiation

Experiment	Model input							Average O/U ratio		Fuel melting	
	Operating history			Fixed parameters			Adjusted parameter q_1 (%)	Model[a]	Exp.[b] (post-irradiation exam)	Model (fuel centreline temperature (K))	Exp. (post-irradiation exam)
	Linear power, P (kW m^{-1})	Post-defect residence time, t (d)	Fuel surface temp., T_1 (K)	Porosity, ε	σ (m^{-1})	Tortuosity, τ					
A. CRL X-2 exps.											
Artificial defects											
FDO-687 (Phase I)	64/55	40/40	870/870	0.0237/0.0237	1350/1350	1.023/1.023	0.18/0.18	2.15/2.14	–/–	Yes (2880)/No (2560)	Yes/No
FFO-103	50	15	870	0.0237	1350	1.023	0	2.17	2.28[c]	Yes (2860)	Yes
Natural defects											
FFO-102-2	67	20	870	0.0237	1350	1.023	0.13	2.16	2.16[d]	Yes (3220)	Yes
FFO-104	58	16	870	0.0237	1350	1.023	43	2.026	2.026[e]	No (2480)	No
B. CANDU spent defective element	~29 (max.) + ~2	~15 + ~40	800 + ~600	0.0237	1350	1.023	0.24	2.044	–	No (1360)	–
				0.0237	1350	1.023	0.24	2.044	2.044[f]	No (620)	No

[a] The model prediction is based on the stated linear power and corresponds to an average value of the radial stoichiometry deviation profile based on a volumetric-average for a cylindrical pellet (see text).
[b] The measured O/U ratio represents an average value for approximately a single pellet sample.
[c] Measured at the mid-length position of element A3N.
[d] Measured between the secondary and main defect area of element A7E (~40 mm from the bottom end of the fuel element).
[e] Measured at the mid-length position of element A2F.
[f] Measured value obtained from Ref. [45].

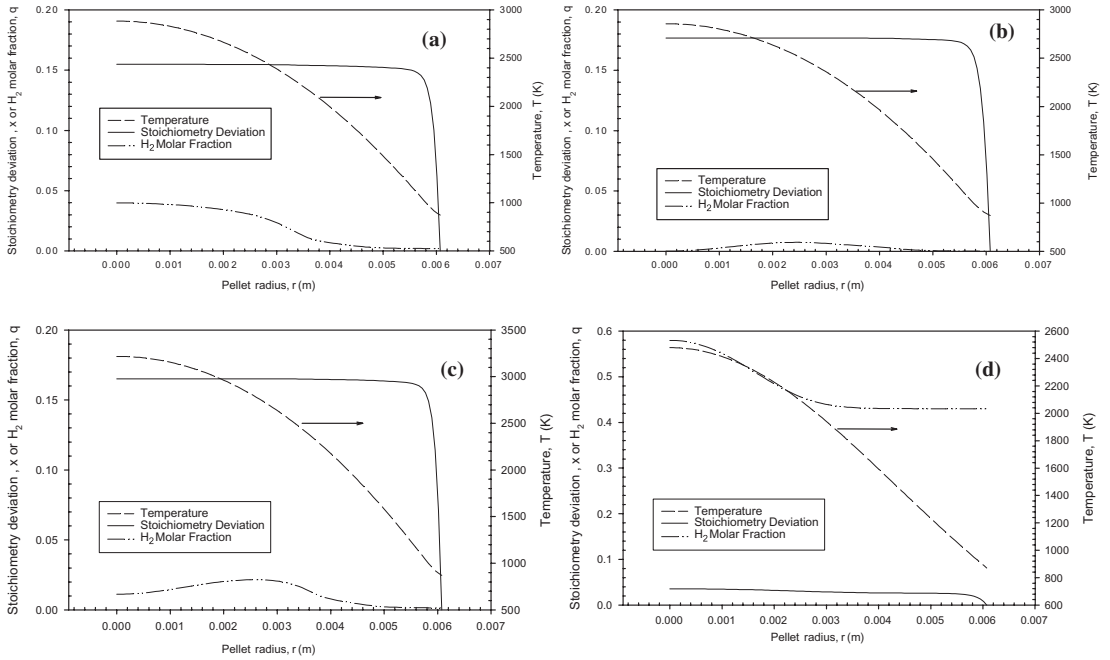

Fig. 8. FEMLAB model predictions of the profiles of the hydrogen mole fractions, stoichiometry deviations and fuel temperatures for (a) FDO-687, (b) FFO-103, (c) FFO-102-2 and (d) FFO-104.

reached (see Fig. 9). The tortuosity τ was obtained by fitting the model to the experimental results of FFO-103, where it was assumed that pure steam is present in the fuel-to-clad gap for the multi-slit rod, i.e., $q_1 \sim 0$. The fuel surface temperature T_1 was set at 870 K based on the ELESIM results. The parameter τ was therefore adjusted until a maximum value of the (pellet-average) stoichiometry deviation was reached. This procedure yielded a value of $\tau \sim 1.023$ and pellet-average O/U ratio of 2.17 (compared to a measured ratio of 2.28). As such,

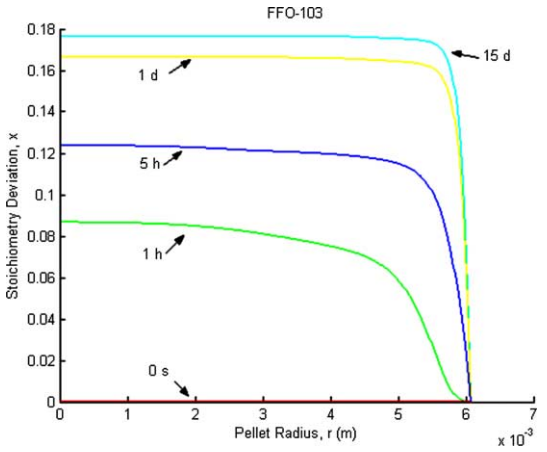

Fig. 9. Stoichiometry deviation profiles for FFO-103 as a function of time.

the model was able to predict the suggested fuel centreline melting seen in FFO-103 (Table 4), with a maximum fuel temperature of 2860 K at a fuel linear rating of $\sim$50 kW m^{-1}. Fuel melting occurs at this temperature due to a reduced solidus and liquidus temperature in the hyper-stoichiometric fuel as illustrated in the phase diagram of Fig. 3 (Fig. 10).

For the other simulations, the previously derived value of τ was used. Since the fuel surface temperature T_1 did not change significantly with linear power in the ELESIM analysis (i.e., typically within $\sim$150 K), this parameter was also conservatively kept constant at 870 K for the other experiments. Thus, the only adjustable parameter in the model is the hydrogen mole fraction in the fuel-to-clad gap, q_1 (which depends on the defect characteristics and the fuel and clad oxidation rates). Hence, for experiments FFO-102-2 and FFO-104, the value of q_1 was adjusted to match the post-test measured stoichiometry deviations (Table 4). Melting was subsequently predicted for the very high-powered element in FFO-102-2, whereas no melting was predicted for FFO-104 as supported by the cermographic examination. For FDO-687, the value of q_1 was also adjusted to match the suggested experimental observation of fuel centreline melting at 64 kW m^{-1} in Phase I for element RPR (Table 3(panel A)). Interestingly, using this fixed value of q_1 no melting is predicted to occur at 55 kW m^{-1} for the other element in this experiment as also observed [44]. Consequently, no fuel melting would be expected for drilled

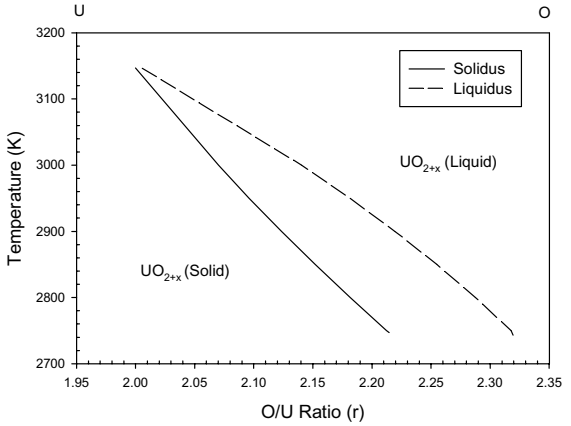

Fig. 10. Solidus and liquidus temperatures for the U–O binary phase diagram as predicted in Fig. 4 (for the hyper-stoichiometry side).

elements as well at an even lower power of 48 kW m^{-1}, as demonstrated in the previous experiment FDO-681 (Table 3(panels A and B)). In addition, if fuel oxidation effects are ignored, no melting is further predicted with the model for the fuel rods RPL and RPP (which were used in FDO-681) that had operated intact at higher powers from 60 to 75 kW m^{-1} in an earlier irradiation.

In summary, the model is able to reasonably match the available O/U measurements and observed melting behaviour (Table 4). This behaviour is related to the defect size and the amount of steam available in the fuel-to-clad gap, i.e., the atmospheric oxygen potential of the gas mixture. For instance, in the multi-slit test of FFO-103 where there is unrestricted coolant entry such that $q_1 = 0$, melting occurs at a relatively lower power of ~50 kW m^{-1}. On the other hand, for the other artificially (FDO-687) and naturally (FFO-102-2) defected elements, the defect sizes were more restricted so that some hydrogen is available in the gap (i.e., due to clad and fuel oxidation processes), where q_1 is typically of the order of ~0.1%. As such, melting does not occur at this same linear rating of 48 kW m^{-1} in the drilled elements of FDO-681. On the other hand, in FFO-104, with small hydride cracks where coolant entry appeared to be more restricted (as evidenced by a relatively low measured O/U ratio of 2.026 and a higher suggested H_2 mole fraction of $q_1 \sim 40\%$), no melting was observed or predicted at 58 kW m^{-1}.

3.2. Simulation of a spent commercial defective element

Similarly, the post-defect irradiation of a fuel element from a commercial CANDU reactor has been simulated with the FEMLAB model (Fig. 11(a)). The simulation can be compared to a measured O/U profile as determined by a coulometric titration method and with ceramography performed during a post-irradiation examination at the CRL (Fig. 11(b)) [45].

Unfortunately, the post-defect residence time was not clearly established for this element, where it was speculated that the element had remained in the defect state for greater than ~10 d. In addition, the irradiation was not typical, where after a period of operation from 23 to 29 kW m^{-1}, the bundle was shifted to an outer channel position where it remained for 40 d at a very low power of ~2 kW m^{-1} [46]. Thus, in the simulation, the rod was assumed to operate at 29 kW m^{-1} for ~15 d, after which the model was re-started (i.e., with the profile obtained from the end of the 15-d simulation) for a remaining irradiation at 2 kW m^{-1} for 40 d. For this lower-powered element, the fuel surface temperature was taken as ~800 K during the first irradiation at 29 kW m^{-1} and ~600 K during the second operating period at 2 kW m^{-1}. The same fixed values of the model parameters of τ, ε and σ as in Section 3.1 were assumed (Table 4).

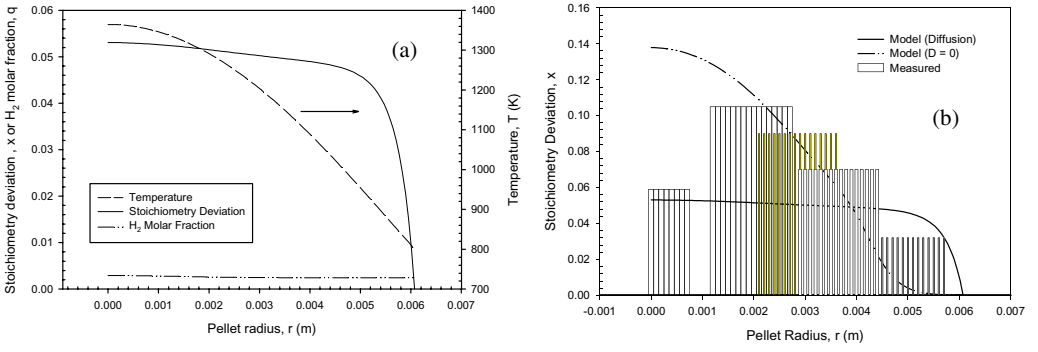

Fig. 11. (a) FEMLAB model predictions of the profiles of the hydrogen mole fractions, stoichiometry deviations and fuel temperatures for a spent defective CANDU fuel element. (b) Comparison of measured and model predictions of the stoichiometry deviation profile. The model predictions are shown with solid-state diffusion and without diffusion. All curves yield a pellet-average stoichiometric deviation of 0.044.

The value of q_1 was again adjusted to reproduce the averaged measured O/U ratio of 2.044 (Table 4). Due to the low temperatures experienced during the second period of operation at 2 kW m^{-1}, no significant diffusion or oxidation occurred so that the stoichiometry deviation profile did not change from that which had occurred in the previous higher-power period. Interestingly, the fitted value of q_1 (i.e., ~0.2%) is close to that obtained for the drilled (FDO-687) and naturally (FFO-102-2) defected elements, where some fuel exposure had also occurred (Table 4).

In Fig. 11(b), it can be seen that the measured O/U profile (i.e., near the secondary defect site) is more peaked than that which is predicted by the model. The model indicates that the stoichiometry deviation profile should flatten out during irradiation as a result of interstitial oxygen diffusion via the chemical diffusion coefficient. A more peaked profile is predicted with the model when solid-state diffusional effects are ignored.

4. Discussion

The discrepancy in the O/U profile shown in Fig. 11 may perhaps be explained by localized sampling of cracks where higher-oxide phases are present due possibly to post-shutdown operations (Fig. 12). For instance, it is conceivable that some of the observed oxidation in the post-irradiation examination (i.e., higher-oxide states) could have been produced after reactor shutdown perhaps during long-term fuel storage in pools (which contain dissolved oxygen), as well as from fuel transfer and shipping operations (where moist air may be present) [19].

In particular, at lower temperatures (i.e., less than ~400 °C), the presence of oxygen, with the presence of perhaps moisture and gamma radiation, may lead to formation of the higher oxides U_4O_9, U_3O_7 and U_3O_8 [47–51]. At lower temperatures, the possibility for solid-state diffusion of oxygen into the solid is significantly reduced. Hence, if defective fuel were exposed to moist air or to water containing dissolved air during post-shutdown operations, the kinetic reactions would be relatively slow (at the lower temperatures) and therefore one would only expect to see localized oxidation with the presence of perhaps higher oxides on exposed fuel surfaces. Interestingly, in the recent ceramography of the defective fuel rod, higher-oxide states were seen locally, typically on exposed surfaces at pellet interface positions and along radial cracks (Fig. 12) [45]. Moreover, higher-oxide states do not occur at higher temperatures during in-reactor operation due to thermodynamic constraints (especially in the presence of hydrogen generated during fuel and cladding oxidation). If the O/U ratios that are measured in the post-irradiation examination are higher than that which had actually occurred during in-reactor operation, a fitting of the model to these measured results would result in conservative predictions of the fuel temperatures as well as a possible overprediction of the extent of fuel centreline melting.

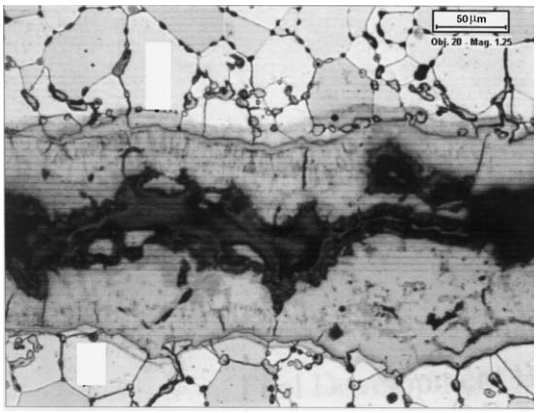

Fig. 12. Ceramography at the centre of the pellet along the pellet interface position showing the presence of higher oxides for the defective fuel element [45].

The current model requires a priori the H_2 mole fraction q_1 in the gas mixture of the gap as a boundary condition. This quantity can be achieved more fundamentally by coupling the given fuel oxidation equations to a gap transport model which accounts for steam penetration through the defect site(s), in order to determine the axial distribution of the oxygen potential in the fuel-to-clad gap [52]. A linked two-dimensional (radial/axial) gap transport/fuel oxidation model is currently under development.

Finally, the surface-exchange coefficient α in Eq. (17) is only strictly applicable to oxidizing conditions. However, in the presence of a reducing atmosphere, the stoichiometry kinetics are observed to be much more rapid as the physical process for removal of oxygen are different [14]. This enhanced process may result from either diffusion through the solid fuel, chemical reaction with hydrogen at the fuel surface or by mass transport through the boundary layer. Hence, neglecting the more rapid kinetics that result during fuel reduction should yield a more conservative estimate of the fuel oxidation state in the current analysis.

5. Conclusions

1. A thermodynamic model of the U–O binary system has been constructed. The U–O model describes the phase equilibrium in the range 25–3000 °C for O/U-proportion ratios ranging from pure U to UO_3. Attention was paid particularly to representing the non-stoichiometry in the solid and liquid 'UO_2' phase and the relation to oxygen partial pressure to support fuel oxidation kinetics modelling (item 2).

2. A model has been developed to account for the fuel oxidation kinetics in operating defective fuel rods. This theoretical representation links the thermodynamic treatment in item 1 (which details the equilibrium state of the fuel) with mass-transport considerations. In particular, the model considers interstitial oxygen diffusion in the solid, and hydrogen generated as a result of the fuel oxidation process and its gas-phase transport in the fuel cracks. As such, an estimate is made of the local oxygen potential throughout the cracked solid. The fuel oxidation model is also coupled to a heat conduction model to enable a calculation of the temperature profile (with fission heating), in which there is a feedback effect due to a degraded thermal conductivity in the hyper-stoichiometric fuel. The physically-based equations of the model have been solved using a finite-element technique with the FEMLAB commercial software package.

3. The model in item 2 has been used to interpret the thermal performance of defective fuel. In particular, the model has been fit to available data from several in-reactor loop experiments with defective fuel. This analysis has provided an estimate of the hydrogen-to-steam partial pressure ratio in the gap that is required to reproduce the (pellet-average) oxygen-to-uranium (O/U) ratio measured by gravimetric analysis. The defect characteristics will significantly influence the hydrogen-to-steam ratio in the fuel-to-clad gap that, in turn, will directly affect the local atmospheric oxygen potential and fuel thermal performance. Higher-powered defective fuel elements will reach a steady-state oxidation state (i.e., under the defect site) in about a day of in-reactor operation. The model has been further benchmarked against an O/U profile measurement (i.e., using a coulometric titration method) of a defective fuel element discharged from a commercial reactor. It is not clear, however, if the measured profile is affected by post-shutdown operations (such as fuel transfer in air or long-term pool storage in pools containing dissolved oxygen).

Acknowledgements

The authors would like to acknowledge helpful discussions with Drs R.A. Verrall and Z. He (CRL) on experimental O/U profile determination and ceramography examination. This work was sponsored by the CANDU Owners Group (COG) under work package WP 22324, the Natural Sciences and Engineering Research Council (NSERC) of Canada and the Director General of Nuclear Safety.

References

[1] P.-Y. Chevalier, E. Fischer, B. Cheynet, J. Nucl. Mater. 303 (2002) 1.
[2] C. Guéneau, M. Baichi, D. Labroche, C. Chatillon, B. Sundman, J. Nucl. Mater. 304 (2002) 161.
[3] P.E. Blackburn, J. Nucl. Mater. 46 (1973) 244.
[4] T.B. Lindemer, T.M. Besmann, J. Nucl. Mater. 130 (1985) 473.
[5] C.W. Bale, A.D. Pelton, W.T. Thompson, Facility for the Analysis of Chemical Thermodynamics, McGill University and École Polytechnique, 1995.
[6] M.H. Kaye, W.T. Thompson, B.J. Lewis, S. Sunder, R. O'Connor, in: 10th International Symposium on Thermodynamics of Nuclear Materials (STNM-10), Halifax, Nova Scotia, 6–11 August 2000.
[7] M.H. Kaye, W.T. Thompson, B.J. Lewis, S. Sunder, R. O'Connor, in: 7th International Conference on CANDU Fuel, Kingston, Ontario, 23–27 September 2001.
[8] B.J. Lewis, R.D. MacDonald, N.V. Ivanoff, F.C. Iglesias, Nucl. Technol. 103 (1993) 220.
[9] B.J. Lewis, F.C. Iglesias, D.S. Cox, E. Gheorghiu, Nucl. Technol. 92 (1990) 353.
[10] B.J. Lewis, B. Andre, B. Morel, P. Dehaudt, D. Maro, P.L. Purdy, D.S. Cox, F.C. Iglesias, M.F. Osborne, R.A. Lorenz, J. Nucl. Mater. 227 (1995) 83.
[11] D.S. Cox, F.C. Iglesias, C.E.L. Hunt, N.A. Keller, R.D. Barrand, J.R. Mitchell, R.F. O'Connor, in: Proceedings of the Symposium on Chemical Phenomena Associated with Radioactivity Releases during Severe Nuclear Plant Accidents, NUREG/CP-0078, Anaheim, CA, 1986, US Nuclear Regulatory Commission, p. 2-35.
[12] D.S. Cox, F.C. Iglesias, C.E.L. Hunt, R.F. O'Connor, R.D. Barrand, in: Proceedings of the International Symposium on High-Temperature Oxidation and Sulphidation Process, Hamilton, Ontario, Canada, 26–30 August 1990.
[13] D.R. Olander, J. Nucl. Mater. 252 (1998) 121.
[14] J. Abrefah, A. de Aguiar Braid, W. Wang, Y. Khalil, D.R. Olander, J. Nucl. Mater. 208 (1994) 98.
[15] M. Imamura, K. Une, J. Nucl. Mater. 247 (1997) 131.
[16] B.V. Dobrov, V.V. Likhanskii, V.D. Ozrin, A.A. Solodov, M.P. Kissane, H. Manenc, J. Nucl. Mater. 255 (1998) 59.
[17] R.A. Verrall, J.F. Mouris, in: 7th International Conference on CANDU Fuel, vol. 2, ISBN 0-919784-71-2, Kingston, Ontario, 23–27 September 2001, Canadian Nuclear Society, 2001.
[18] B.J. Lewis, B. Szpunar, F.C. Iglesias, J. Nucl. Mater. 306 (2002) 30.
[19] D.R. Olander, Y.S. Kim, W. Wang, S.K. Yagnik, J. Nucl. Mater. 270 (1999) 11.
[20] D.R. Olander, Nucl. Technol. 74 (1986) 215.
[21] W.E. Wang, D.R. Olander, J. Am. Ceram. Soc. 65 (5) (1993) 1242.
[22] D. Labroche, O. Dugne, C. Chatillon, J. Nucl. Mater. 312 (2003) 21.
[23] J.L. Bates, J. Am. Ceram. Soc. 49 (7) (1966) 396.
[24] R.G. Ackermann, E.G. Rauh, M.S. Chandrasekharaiah, J. Phys. Chem. 34 (4) (1969) 762.
[25] R.K. Edwards, A.E. Martin, in: Thermodynamics of Nuclear Materials, vol. 2, IAEA, Vienna, 1966, p. 423.
[26] P.E. Balckburn, J. Phys. Chem. 62 (8) (1958) 897.
[27] B.E. Schanner, J. Nucl. Mater. 2 (2) (1960) 110.
[28] L.E.J. Roberts, A.J. Walter, J. Inorg. Nucl. Chem. 22 (1961) 213.

[29] S. Aronson, J.E. Rulli, B.E. Schanner, J. Phys. Chem. 35 (4) (1961) 1382.
[30] M.J. Bannister, W.J. Buykx, J. Nucl. Mater. 55 (1974) 345.
[31] Y. Saito, J. Nucl. Mater. 51 (1974) 112.
[32] A. Nakamura, T. Fujino, J. Nucl. Mater. 149 (1987) 80.
[33] A.E. Martin, R.K. Edwards, J. Phys. Chem. 69 (5) (1965) 1788.
[34] R.E. Latta, R.E. Fryxell, J. Nucl. Mater. 35 (1970) 195.
[35] A.M. Anthony, R. Kiyoura, T. Sata, J. Nucl. Mater. 10 (1) (1963) 8.
[36] A. Kotlar, P. Gerdanian, M. Dode, J. Chim. Phys. 65 (1968) 687.
[37] O. Kubaschewski, C.B. Alcock, Metallurgical Thermochemistry, 5th Ed., Pergamon, New York, 1979.
[38] J.A. Meachen, Nucl. Energy 28 (4) (1989) 221.
[39] R.B. Bird, W.E. Stewart, E.N. Lightfoot, Transport Phenomena, Wiley, New York, 1960.
[40] R.C. Reid, J.M. Prausnitz, B.E. Poling, The Properties of Gases and Liquids, McGraw-Hill Book Company, New York, 1987.
[41] D.R. Olander, Fundamental aspects of nuclear reactor fuel elements, TID-26711-p1, US Department of Energy, 1976.
[42] W.E. Ellis, J.D. Porter, T.L. Shaw, in: Proceedings of the International Topical Meeting on Light Water Reactor Fuel Performance, Park City, Utah, 10–13 April 2000, p. 715.
[43] FEMLAB User's Guide and Introduction, COMSOL, Burlington, MA, USA, 2001.
[44] R.D. MacDonald, J.J. Lipsett, E.E. Perez, P.K. Kos, Atomic Energy of Canada Limited report, AECL-7751, May 1983.
[45] Z. He, R.A. Verrall, J. Mouris, C. Buchanan, in: 8th International Conference on CANDU Fuel, Honey Harbour, Ontario, 21–24 September 2003.
[46] E. Kohn, M. Notley, private communication, 2002.
[47] P. Taylor, D.D. Wood, D.G. Owen, J. Nucl. Mater. 183 (1991) 105.
[48] P. Taylor, R.J. Lemire, D.D. Wood, Nucl. Technol. 104 (1993) 164.
[49] S. Sunder, N.H. Miller, J. Nucl. Mater. 231 (1996) 121.
[50] R.J. McEachern, J. Nucl. Mater. 245 (1997) 238.
[51] R.J. McEachern, P. Taylor, J. Nucl. Mater. 254 (1998) 87.
[52] B.J. Lewis, in: 6th International Conference on CANDU Fuel, vol. 1, ISBN 0-919784-62-3, Niagara Falls, Ontario, 26–29 September 1999, p. 403.